Full length article

[INVITED] Subwavelength structures for silicon photonics biosensing ☆

J. Gonzalo Wangüemert-Pérez [a,*], Abdelfettah Hadij-ElHouati [a], Alejandro Sánchez-Postigo [a], Jonas Leuermann [a,b], Dan-Xia Xu [c], Pavel Cheben [c], Alejandro Ortega-Moñux [a], Robert Halir [a,b], Íñigo Molina-Fernández [a,b]

[a] Departamento de Ingeniería de Comunicaciones, ETSI Telecomunicación, Universidad de Málaga, Campus de Teatinos s/n, 29071 Málaga, Spain
[b] Bionand Center for Nanomedicine and Biotechnology, Parque Tecnológico de Andalucía, 29590 Málaga, Spain
[c] National Research Council Canada, Ottawa, Ontario K1A 0R6, Canada

A B S T R A C T

Silicon photonic biosensors hold the potential for highly accurate, yet low cost point-of-care devices. Maximizing the sensitivity of the sensing chips while reducing the complexity and cost of the read-out system is pivotal to realize this potential. Here we present an extensive analysis, both from a practical and a theoretical perspective, of current biosensors, and analyze how subwavelength structures can be exploited to enhance their sensitivity. This study is not restricted just to the near-infrared band as we also determine the sensing capabilities of the suspended silicon waveguides with subwavelength metamaterial cladding working in the mid-infrared range. These waveguides have been recently proposed to cover the full transparency window of silicon ($\lambda < \sim 8.5\ \mu m$), where the fingerprint spectral region of many molecules takes place and so a plethora of evanescent field absorption-based applications will be developed in the near future.

1. Introduction

Silicon photonic biosensors are capable of detecting trace amounts of biomolecules, such as antibodies and proteins, and can monitor their reactions in real-time, without prior labeling of the targets [1,2]. Combined with their ability to detect several different analytes in parallel in a single chip, this makes them ideally suited for early diagnosis of diseases [3–5] and drug discovery [6,7]. They are also considered promising candidates for the development of lab-on-chip platforms and point-of-care devices. The basic principle underlying their operation is evanescent field sensing, illustrated in Fig. 1. The surface of an optical waveguide is functionalized with receptor biomolecules, which bind, with high specificity, to the analyte [8], e.g. antibodies that will attach only to their corresponding antigens. When an aqueous solution containing the analyte flows over the waveguide, the analyte will bind to the receptors on the waveguide surface, locally changing its optical properties. Light propagating through the waveguide is confined by total internal reflection, but 'senses' the medium surrounding the waveguide through the evanescent tails of its electric field. When a light-wave interacts with the biomolecules that are

binding to the waveguide surface some of its properties (wavelength, amplitude or polarization) change, and by monitoring these changes the analyte can be detected. Thus, while the specificity of photonic biosensors depends mainly on the surface functionalization, their sensitivity strongly depends on their optical implementation. Indeed, over the last decade, extensive research efforts have been devoted to optimizing this sensitivity: different waveguide types, such as silicon wire waveguides, slot waveguides and more recently subwavelength grating (SWG) waveguides have been explored, as well as different sensing architectures, mainly based on ring-resonators and Mach-Zehnder interferometers have been studied.

In this paper we aim to provide both theoretical and practical insight into photonic sensor design, with a particular emphasis on subwavelength structures which can provide some of the highest sensitivities to date. To this end, we start with a systematic description of the waveguide and architectural parameters that govern sensitivity in Section 2. In Section 3, we describe the practical realization of two complete sensing systems: one based on ring-resonators, and one based on interferometry. In Section 4, we systematically analyze, for the first time, the sensitivity of subwavelength grating waveguides, revealing that current design parameters may be sub-optimal. The sensing properties of suspended silicon waveguides, operating in the mid-infrared wavelength range, are discussed, for the first time, in Section 5. Finally we present some concluding remarks.
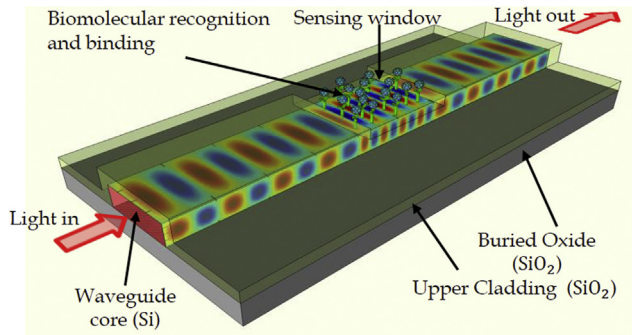
Fig. 1. Photonic wire waveguide for biosensing in the silicon-on-insulator platform.

2. Fundamentals of photonics biosensors

This section lays the theoretical foundation required to understand the parameters that govern the sensitivity and limit of detection of photonic biosensors.

2.1. Waveguide and architecture sensitivity

Fig. 1 illustrates a typical biosensor waveguide in silicon-on-insulator. The waveguide is covered by a protective SiO_2 cladding, except for the sensing window, where the waveguide core is exposed to the surrounding medium. When a sample of the analyte is delivered to the sensing window through a microfluidic channel (not shown in the figure) and gets in touch with the functionalized surface of the waveguide, molecular binding takes place. Interaction of these molecules with the evanescent tail of the guided mode field changes its effective index and thus its wavelength [9]. One of the most important characteristics of a sensor is the waveguide mode sensitivity S_w which maps the physical change due to molecular binding, into effective index variations:

$$S_w = \frac{\partial n_{\text{eff}}}{\partial \Gamma},\tag{1}$$

where $\partial \Gamma$ is the variation of any physical parameter. Unfortunately, the effective index of a waveguide mode is not a directly measurable quantity, so in order to be useful, they must be mapped into a quantity that can be readily detected. This is achieved by using a photonic sensing architecture. These architectures can be broadly categorized in two different configurations: interferometric and resonant [10]. In interferometric architectures the effective index variations are mapped into an optical phase shift, $\Delta \varphi$, while in a resonant architectures they are mapped into a wavelength shift $\Delta \lambda$. Focusing on the interferometric type of sensor, the architecture sensitivity S_a can be defined as

$$S_a = \frac{\partial \varphi}{\partial n_{\text{eff}}},\tag{2}$$

and the total photonic device sensitivity S can be calculated as the product of waveguide and architecture sensitivities

$$S = S_a\,S_w = \frac{\partial \varphi}{\partial n_{\text{eff}}}\,\frac{\partial n_{\text{eff}}}{\partial \Gamma} = \frac{\partial \varphi}{\partial \Gamma}.\tag{3}$$

While this magnitude depends only on the photonic integrated circuit, the limit of detection (LOD), i.e. the minimum amount of detectable variation in the physical parameter $\Delta \Gamma_{min}$, will also depend on the minimum detectable phase shift $\Delta \varphi_{min}$ that can be accurately resolved by the measurement apparatus. This quantity is sometimes referred as the set-up resolution R and can be related to the system noise variance σ_φ through [11]:

$$R = \Delta\varphi_{min} = 3\sigma_\varphi.\tag{4}$$

From these definitions the LOD can be easily calculated as

$$LOD = \Delta\Gamma_{min} = \frac{R}{S_a S_w}.\tag{5}$$

The same type of definition applies to resonant sensors by substituting, in Eqs. (2)–(4), φ by λ.

Since the LOD depends both on the photonic chip and on the resolution of the measurement apparatus, it is difficult to compare the performance of different sensor devices using this metric. Researchers working on resonant sensors therefore make a distinction between the system LOD (sLOD) which depends on the complete set up, and the intrinsic LOD (iLOD) which only depends on the photonic device itself [12]. This distinction will be explained in the Section 2.3. Unfortunately, to the authors' knowledge, no such metrics have been proposed for interferometric biosensors.

2.2. Bulk and surface waveguide sensitivities

Two different waveguide sensitivities are defined in the literature: bulk $S_{w,\,bulk}$ and surface sensitivity $S_{w,\,surf}$.

Referring to Fig. 2(a), bulk sensitivity is defined as the ratio of change of the mode effective index (∂n_{eff}) and the change of the refractive index of the material covering the waveguide (∂n_c)

$$S_{w,\,bulk} = \frac{\partial n_{\text{eff}}}{\partial n_c}\quad (\text{RIU/RIU}).\tag{6}$$

Surface sensitivity is defined as the ratio of the mode effective index change (∂n_{eff}) and the change in thickness (∂t) of the adsorbed molecular layer, as shown in Fig. 2(b)

$$S_{w,\,surf} = \frac{\partial n_{\text{eff}}}{\partial t}\quad (\text{RIU/nm}).\tag{7}$$

These are purely electromagnetic definitions which are very useful for photonic designers. From the chemical point of view, two related magnitudes can be used. Waveguide bulk sensitivity can be also defined as the ratio of effective index variation and the change in the analyte concentration (∂c, in moles per liter or M):

$$S_{w,\,bulk} = \frac{\partial n_{\text{eff}}}{\partial c}\quad (\text{RIU/M}).\tag{8}$$

This measure is only of relative importance for the biomolecular recognition capability of the sensor (which takes place in the sensor surface) but is sometimes used as an intermediate step in sensor characterization. On the other hand waveguide surface sensitivity can be also defined as

$$S_{w,\,surf} = \frac{\partial n_{\text{eff}}}{\partial \rho_s}\left(\frac{\text{RIU}}{\text{pg/mm}^2}\right),\tag{9}$$

where ρ_s is the mass surface density of the adsorbed layer.

Please notice that in all these definitions, it is always assumed that there is enough analyte to completely fill up (cover) all the volume (surface) of the sensing window. For other applications, in which there is a very limited amount of analyte (for example, single molecule detection), other metrics should be used.
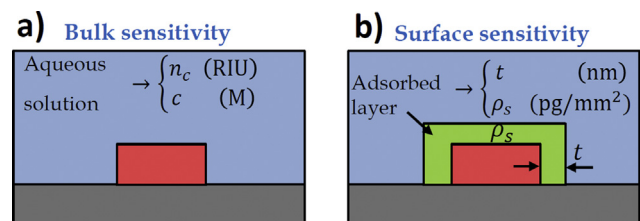

Fig. 2. Bulk and surface sensitivities.

The bulk and surface waveguide sensitivities strongly depend on the geometry of the sensing waveguide. Different types of waveguide geometries have been proposed for biosensing applications. For example, the bimodal waveguide consisting of a 350 nm thick SiN waveguide with a 2 nm ridge has been successfully used for bulk and surface sensing showing state of the art sensitivities [13,1]. While this waveguide is very sensitive, it exhibits reduced lateral mode confinement, which limits integration density. Many different waveguide geometries have been proposed that offer greater integration levels: silicon wires in quasi-TE [14] and quasi-TM [15] polarization (hereafter noted just as TE and TM), slot waveguides [16,17] and subwavelength waveguides [18–23]. Their performance metrics will be summarized in Section 4.3.

2.3. Sensing architectures

Existing photonic biosensing architectures can be broadly classified into interferometric and resonant architectures.

2.3.1. Interferometric sensors

Interferometric sensors have been extensively used by many research groups exhibiting excellent sensitivities [9,1,24]. Many different interferometric architectures can be found in the literature (Mach-Zehnder, Young, Bimodal) but they all share a common sensing principle. As illustrated in Fig. 3(a), in interferometric sensors the light from a laser source is divided into two paths by a power splitter. One of the beams travels through the sensing waveguide interacting with the sample along the interaction distance L, while the other beam is not exposed to the sample and serves as a fixed reference for phase comparison. This produces a phase difference $\Delta\varphi$, at the device output given by

$$\Delta\varphi = \frac{2\pi}{\lambda_0}\Delta n_{\text{eff}}\,L, \tag{10}$$

and thus the architecture sensitivity is

$$S_a = \frac{\partial\varphi}{\partial n_{\text{eff}}} = \frac{2\pi}{\lambda_0}L. \tag{11}$$

Therefore, the interaction length L acts as an amplification factor improving device sensitivity S. In the absence of losses, L could be increased as much as required. In high contrast platforms, allowing low-loss micro-metric bending radii, this can be achieved in a very compact way by using spiral waveguides, with interaction lengths of several millimeters concentrated in a single spot a few hundreds of microns in diameter [25].

To convert the phase difference $\Delta\varphi$ into an electrical signal most existing interferometer sensors use the configuration shown in Fig. 3(b): the reference and sensing beams are added in a power combiner, and passed through a photodetector (PD) which yields a photocurrent:

$$i(t) \propto \cos(\Delta\varphi). \tag{12}$$

The scheme is simple, but as the photocurrent is proportional to the cosine of the phase shift it suffers from ambiguity and sensitivity loss which can be only partially circumvented by slightly modulating the wavelength of the input signal [26].

The aforementioned problems arise not from the interferometric sensing principle itself (measuring of phase difference between the sensing and reference arms) but from a sub-optimal way of extracting this phase. These problems where recognized in [27] where a coherent phase detection scheme, inherited from the optical telecommunication world [28], was proposed to improve device performance – see Fig. 3(c). This scheme has been recently demonstrated showing state of the art bulk sensitivities [29]. As shown in Fig. 3(c), in this architecture, the sensing and reference signals are the input to a coherent receiver [28] that can be implemented with simple 2×4 Multimode Interference Couplers (MMIs) and balanced photodiodes (BPD), although simpler architectures based in 2×3 MMIs do also exist (see Section 3.2). The receiver produces two output photocurrents

$$\begin{aligned}i_i(t) &\propto \cos(\Delta\varphi)\\i_q(t) &\propto \sin(\Delta\varphi),\end{aligned} \tag{13}$$

from which the phase information can be unambiguously obtained with optimum sensitivity.

2.3.2. Resonant sensors

As mentioned previously, spiral waveguides can be used to fit the required interaction length into the available chip surface. However there are some cases in which further size reduction is needed: in applications that require simultaneous measurement of many different reactions with high density arrays [30], or when trying to detect tiny amounts of analyte, as for example, in single molecule detection [31]. In these cases, resonant sensors can provide an interesting alternative to interferometric devices. Many different resonant sensors have been reported based in different structures including rings [14,32], spiral resonators [15], Bragg gratings [33] or disks [34].

In resonant sensors, the sensing waveguide is part of a resonating cavity. Light introduced in the cavity undergoes a large number of round trips along the physical length of the sensing waveguide before exiting the cavity, thus effectively increasing the interaction length. The effective length can be calculated as [1]:

$$L_{\text{eff}} = Q\,\frac{\lambda_0}{2\pi\,n_g}, \tag{14}$$

where λ_0 is the resonator wavelength, n_g is the waveguide group index and the Q factor is related to the resonance 3 dB linewidth through

$$Q = \frac{\lambda_0}{\Delta\lambda_{3dB}}. \tag{15}$$

This enables size reduction without losing sensitivity, but at the cost of increasing the complexity of the detection. Indeed, in resonant architectures the waveguide mode effective index variations are mapped into a resonance wavelength shift, which has to be measured with a tunable laser source or using a spectrum analyzer [11], resulting in a more complex measurement setup compared to interferometric sensors. Moreover, contrarily to interferometric sensors, the architecture sensitivity is almost fixed. Indeed, the shift of the resonance wavelength with waveguide effective index can be written as [12]:

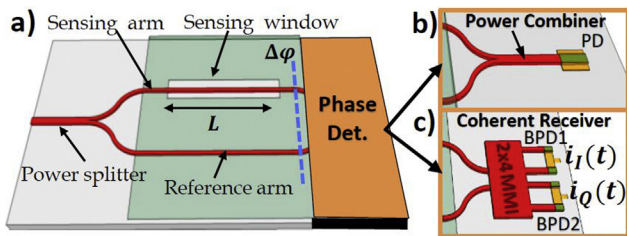$$\Delta\lambda = \frac{\lambda_0}{n_g}\Delta n_{\text{eff}}, \tag{16}$$

Fig. 3. (a) Mach Zehnder interferometer with interaction length L. Variations in the effective refractive index Δn_{eff} of the waveguide mode are mapped to phase variations $\Delta\varphi$ at the output plane (marked as a blue dashed line). Two alternatives for implementing the phase detection block are shown: (b) incoherent phase detection and (c) coherent phase detection. Please note that in most sensor chips the photodetectors are not integrated due to cost constraints. (For interpretation of the references to color in this figure legend, the reader is referred to the web version of this article.)

from where the architecture sensitivity for resonant sensors can be obtained as

$$S_a = \frac{\partial \lambda}{\partial n_{\text{eff}}} = \frac{\lambda_0}{n_g}. \tag{17}$$

This means that the only way to improve sensitivity is to use longer wavelengths or to decrease the waveguide group index. In practical cases the range in which these parameters can be changed is more limited that the interaction length in interferometric devices.

As mentioned in Section 2.1, to obviate the dependence of the LOD with the resolution of the measurement set-up, an intrinsic LOD (iLOD) has been defined for resonator sensors [12]. The iLOD is defined by setting the set-up resolution R equal to one resonator linewidth, i.e. $R = \Delta\lambda_{3dB}$, so that

$$\text{iLOD} = LOD|_{R=\Delta\lambda_{3dB}} = \frac{\Delta\lambda_{3dB}}{S} = \frac{\lambda_o}{Q \cdot S}. \tag{18}$$

Although this figure of merit allows us to establish a comparison between different resonant sensors, it is not useful to compare them with interferometric sensors.

To conclude this section, it is worth highlight an aspect that is not always considered by researchers working on the field of photonic biosensors: losses. Observing Eq. (18) it is clear that to achieve a low iLOD, what is really important is the product $Q \cdot S$, not the device sensitivity. Therefore, the maximization of device sensitivity should not be attained at the cost of a proportional increase of the losses, or equivalently, a reduction of the Q factor.

3. Examples of full sensing systems

In the following we describe two practical photonic sensing platforms, based on ring-resonators, and interferometry, respectively.

3.1. Ring resonators for high throughput measurements

Applications of molecular sensors in genomics, proteolytic and drug screening often require high throughput measurements of many different binding reactions. This need for high throughput multiplexed affinity binding tools with increasing levels of automation is one of the main drivers for instrument development. The sensing readout should be robust and immune to external environmental changes, such as temperature drifts and light intensity fluctuations. The cost of the manufactured sensor array chips should be low enough that the chips can be considered disposable. To be deployable in field testing and in laboratories devoted to biological or medical research, the sensor chip and associated instrumentation need to be self-contained and without stringent requirements on optical alignment, and therefore amenable to operation by users with no specialized expertise in photonics. Furthermore, the sensing surface functionalization and analyte delivery methods should be fully compatible with existing infrastructure in molecular analysis and research. Below we describe a sensing platform developed at the National Research Council Canada (NRC) that fulfills these requirements. Although the sensor chips are based on silicon photonic wire sensors [25], the instrument architecture and the readout system can be readily adapted to other sensor designs such as these employing subwavelength structures. We selected folded spiral cavity resonator design as the basic sensor elements [35]. A lengthened cavity relaxes the critical coupling condition to the optical cavity and provides stable resonance contrast and high quality factors which are only weakly affected by waveguide loss or coupling variations. This feature is beneficial for multiple sensor arrays where the reference and the sensing elements are required to be nominally identical. Sensor elements are formed using 450 nm wide silicon photonic wire waveguides etched in a 260 nm thick silicon layer, operating in TM mode. An SU8 polymer layer of 2 μm-thick was used to isolate the chip from the environment, patterned such to expose only the sensing elements to the aqueous analyte. On every sensor array, 1–4 sensors were used as a temperature Ref. [36], and for these sensor the SU8 layer was left in place over the resonator waveguide. Real-time measurements show that the reference resonator resonances reflect the temperature changes without noticeable time delay, enabling effective cancellation of temperature-induced shifts. A second 50 μm thick SU8 layer was lithographically patterned to define the microfluidic channels, which were terminated at both ends by an 800 μm wide reservoir that aligns with the inlet and outlet apertures on the reader instrument fluidic manifold. Due to the high index contrast, a long waveguide cavity of over 1 mm can be fitted within a small area of 100 μm in diameter and achieving a Q of 20,000. The sensor arrays of up to 128 elements occupy an area of approximately 2 mm × 2 mm. The overall chip size is mainly determined by requirements for the fluidic channels. The size and layout of the sensor array is fully compatible with commercial spotting tools designed to independently functionalize fluorescence based biochips.

The readout system is illustrated in Fig. 4 [15], and the insert shows a spiral resonator sensor within the sensing window and fluidic channel formed in SU8. Light is coupled to and from the chip waveguides using the sub-wavelength patterned grating couplers [37,38]. The advantage of the sub-wavelength patterning approach for grating couplers is that all waveguides, sensor elements and the grating couplers are fabricated in the same lithography and etch step. Thus manufacturing is simpler, yet it still is compatible with publicly available foundry services using DUV lithography handling eight inch wafers [39]. Using fabrication technologies compatible with volume production provides large number and low cost chips needed for biological assay development. During measurement, the sample liquids is delivered to the chip via a peristaltic pump and flowed over the sensor elements, while the optical signals from each sensor in the array are continuously monitored. The system is capable of acquiring up to 128 optical sensor outputs simultaneously and in real time. The features described above in the chip, fluidics and the reader instrument allowed automated optical alignment of the silicon sensor chip with the input beam and output acquisition optics, as well as automated connection of the fluid delivery system. For benchmarking, binding between complementary IgG protein pairs was monitored over 4 orders of magnitude dynamic range down to a concentration of 20 pM, demonstrating a resolvable mass of 40 attograms [35].
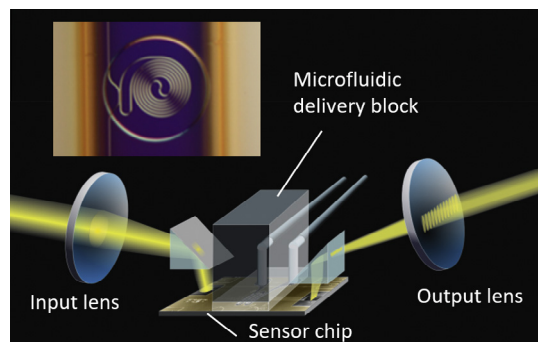

Fig. 4. A schematic diagram showing the sensor chip, microfluidic block, and input and output lenses within the reader instrument. Dimensions shown are not to scale. The output beams are focused onto an InGaAs detector array to the right (not shown). The insert shows a spiral resonator sensor element within the sensing window and fluidic channel formed in SU8.

The microarray system was then used to demonstrate a multiplexed assay for serotyping *E. coli* bacteria. Five groups of sensors were functionalized using serospecific polyclonal antibody probe molecules (O121, O145, O55, O103 and O157 respectively) to distinguish between five different *E. coli* O-serotypes. When passing the sample liquid containing O55 bacteria, only the sensor with O55 probes showed significant response [15]. The experiment demonstrates that this microarray platform can perform rapid multiplexed serotyping tests to identify *E. coli* and other pathogens, using a low cost disposable chip. This type of affinity binding test can be faster and provide multiplexed throughput, be more quantitative, and can use significantly less antibodies than agglutination based serotyping methods.

3.2. Interferometric sensors with coherent phase read-out

As described in Section 2 there are various types of detection architectures to read-out the phase shift induced in the sensing arm of an MZI. Some suffer sensitivity fading and directional ambiguity as they only consider the In-Phase interferometric signal, $I(t)$ [26]. To overcome these issues an advanced phase-readout technique, based on techniques originally developed for coherent optical communications [40], was proposed in [27]. Using a 2×3 Multimode Interference Coupler (MMI) access to the Quadrature-Phase, $Q(t)$, interferometric signal is gained, thereby improving the sensor read-out. A sensing chip based on this approach was designed in silicon nitride technology, and is schematically illustrated in Fig. 5. Silicon nitride has low absorption losses from the visible to the mid-infrared wavelengths, therefore providing a versatile platform to detect biochemical interactions. Judiciously designed sensing waveguides in SiN exhibit good bulk sensitivities while maintaining strong guiding characteristics in the lateral dimension. Furthermore, since silicon nitride may be integrated with CMOS manufacturing techniques, low cost and high volume fabrication is feasible.

To progress in the field of photonic biosensing technologies a photonic setup with integrated microfluidic channel for biochemical characterizations has been implemented at BIONAND Andalusian Centre for Nanomedicine & Biotechnology in cooperation with the University of Málaga. A schematic view of the assembled setup is shown in Fig. 5. The monochromatic C-Band LASER source ($\lambda = 1550$ nm) with a maximum output power of 15 dBm is linked to a polarization rotator which in turn is connected to a fiber array (FA). Located above the photonic integrated chip (PIC), the TE polarized beam couples into the PIC through surface grating couplers with an estimated coupling efficiency (CE) of -5 dB at a

radiation angle of 33°. The coupled light is split by an 1×2 MMI between the reference and sensing arm of the interferometer. The microfluidic channel above the sensing window of the PIC provides access to the sensing area for analyte which is dissolved in a specific buffer (e.g. de-ionized water). Only light in the sensing arms interacts with the analyte, while the light in the reference arm propagates unaltered. In the 2×3 MMI, the lightwaves from both arms recombine and interfere in the three output waveguides. These outputs are coupled back to the FA and are detected by separate photodiodes. The photodiodes and the consecutive transimpedance amplifiers (TIA) convert the received optical intensity into an equivalent voltage which is recorded with a data acquisition card (DAQ). The complex signal (I-Q) recovered by digital signal processing (DSP) enables the reconstruction of the unwrapped accumulated phase change in the sensing arm, as detailed in the next paragraph.

Generally, N×M MMIs divide light from of a certain input $i \in \{1, \ldots, N\}$ equally between the M different output waveguides with distinctive phase shifts φ_k with $k \in \{1, \ldots, M\}$. MMIs are widely used in integrated optics due to their good performance and relaxed fabrication tolerances in comparison to other integrated splitting devices [41]. In the specific case of a 2×3 MMI it splits both incoming modes uniformly between the three output waveguides, and light from the two inputs recombines with phase differences shifted by 120° at each output. The power received at each output $k = \{1, 2, 3\}$ (see Fig. 5) is then given by:

$$P_{opt,k}(t) = \frac{P_0}{3} \cdot \left(1 + V_{Vis} \cos \left(\varphi(t) + \frac{2\pi(k-1)}{3} \right) \right), \qquad (19)$$

where $\varphi(t)$ is the accumulated phase difference between both incoming modes, V_{Vis} the visibility of the interferometric signal and P_0 a power scaling constant. The In-Phase and Quadrature-Phase interferometric signals may be recovered by $P_{opt,k}(t)$ according to [28],

$$
\begin{aligned}
I(t) &= 2 \cdot P_{opt,2}(t) - P_{opt,1}(t) - P_{opt,3}(t) \\
Q(t) &= \sqrt{3} \cdot (P_{opt,1}(t) - P_{opt,3}(t)),
\end{aligned}
\qquad (20)
$$

from where the signal $S(t) = I(t) + i \cdot Q(t) = P_0 P_{Vis} \cdot \exp(i \cdot \varphi(t))$ is calculated, with $i = \sqrt{-1}$. Ideally $S(t)$ describes a perfect circle in the I-Q-Plane. Fabricated devices are normally subject to small variations in waveguide thickness and width. These variations, together with the uncertainty in the alignment of the fiber array, will influence each output path of the 2×3 MMI, resulting in different power scaling factors, visibilities, and phase shifts. Without proper calibration the accumulated phase difference $\varphi(t)$ may then not be appropriately recovered. To compensate those effects blind calibration schemes have been developed in the last years to recover the correct phase readout [27,42]. An example of a calibration is shown in Fig. 6 for which an uncalibrated complex signal $S_{rec}(t)$ (red curve) has been recorded while a drop of water entered the sensing window of the MZI describing a shifted (I_s, Q_s) and rotated (α) ellipse in the I-Q-Plane. The corresponding calibrated signal $S_{cal}(t)$ (represented in blue) is calculated by applying a linear transformation to $S_{rec}(t)$ restoring the desired shape.

From a theoretic point of view the bulk device sensitivity (S_{bulk}) of the proposed MZI based coherent 2×3 multiport sensing architecture must be calculated according to Eq. (3), which, combined with Eq. (6) and (11), becomes:

$$S_{bulk} = S_a \cdot S_{w,bulk} = \frac{2\pi}{\lambda_0} \cdot L \cdot \frac{\partial n_{eff}}{\partial n_c} \qquad \left(\frac{\text{rad}}{\text{RIU}} \right) \qquad (21)$$

where $\lambda_o = 1550$ nm and $\partial n_{eff}/\partial n_c$ is designed to be 0.22. Several MZI structures have been integrated on the PIC with different lengths, from L $\approx$ 0.5 cm up to L $\approx$ 2.2 cm, which determines the
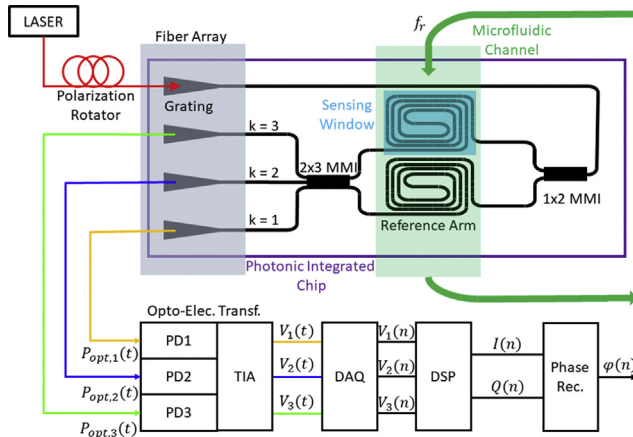

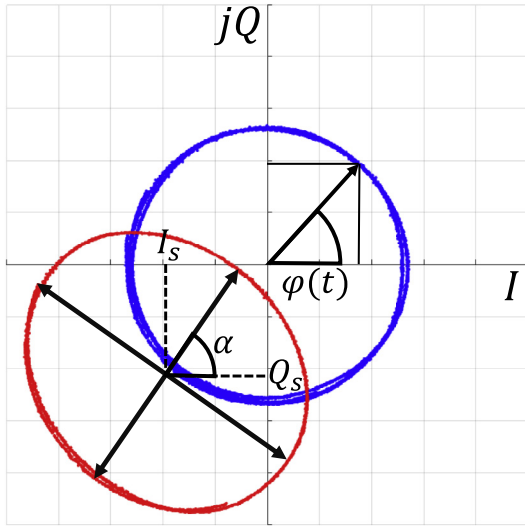**Fig. 5.** Schematic view of the photonic setup with microfluidic channel.

Fig. 6. Illustration of an uncalibrated (red) and corresponding calibrated (blue) complex signal. (For interpretation of the references to color in this figure legend, the reader is referred to the web version of this article.)

corresponding sensitivities in the range of $1.42\pi \cdot 10^3$ rad/RIU to $6.23\pi \cdot 10^3$ rad/RIU. However, fabrication imperfections may affect $\partial n_{eff}/\partial n_c$. Therefore, besides calibrating the readout, the sensing architecture itself must be calibrated as well to determine the bulk sensitivity S_{bulk}. Different groups have done calibration following the same procedure, flowing solutions with known refractive indices n_p through the microfluidics. The measured phase shifts φ_p are used to fit a linear regression curve whose slope is the bulk sensitivity. In literature numerous compounds for evaluating the sensitivity can be found, such as hydrogen chloride (HCl) [43], glucose ($C_6H_{12}O_6$) [44] or sodium chloride (NaCl) [29]. According to Eq. (5) the limit of detection (LOD) may also be determined after calibration.

4. SWG based photonic biosensors

Through this section we will present the potential of diffractionless subwavelength grating (SWG) waveguides for sensing applications, by demonstrating its powerful capability to engineer the spatial distribution of the mode profile, and thereby maximizing the light-matter interaction. This study will also reveal that the waveguide dimensions used until now by some researchers are not optimum from the sensitivity point of view. We will finish the section providing a summary of the performance metrics attained by recently published works of photonic biosensors that employ subwavelength periodic structures as sensing waveguides.

4.1. The subwavelength grating waveguide

A schematic representation of a SWG waveguide is shown in Fig. 7. The homogeneous silicon core of the conventional photonic wire is replaced by a periodic arrangement of silicon blocks. The geometrical parameters describing this structure are: the waveguide width (W), the silicon layer height (H), the period or pitch (Λ) and the duty cycle ($DC = L_{Si}/\Lambda$). Depending on the size of the period (Λ) compared to the free-space wavelength (λ_0), three different operating regimes exist: i) subwavelength, where the pitch is small enough to suppress diffraction effects ($\Lambda < \frac{\lambda_0}{2 \cdot n_{eff}}$) and the structure behaves as a lossless waveguide whose core can be modeled as an homogeneous anisotropic material [45]; ii) Bragg or
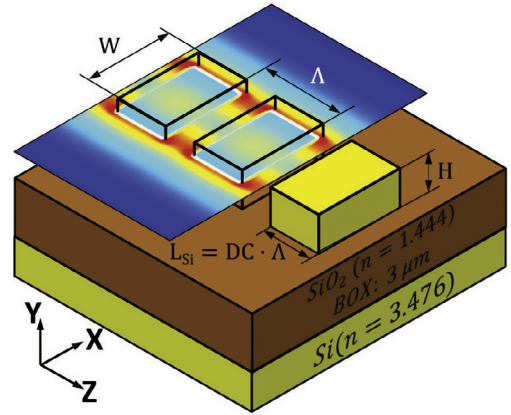

Fig. 7. Schematic representation of a SWG waveguide. The electric field intensity distribution in the XZ plane is shown at half-height of the silicon blocks.

photonic band gap, where the incoming light is completely reflected backwards ($\Lambda = \frac{\lambda_0}{2 \cdot n_{eff}}$); and iii) diffraction, where the light is gradually radiated as it travels through the periodic waveguide [46]. In all cases, the electromagnetic field solutions supported by the structure can be rigorously described by the Floquet-Bloch modes formalism [47].

Operation in the subwavelength regime is very attractive in the field of photonics integrated circuits because, by using a single etch-depth and judiciously choosing the aforementioned geometrical parameters, it is possible to control the properties of the Floquet-Bloch mode. Not only is it feasible to tailor its effective index, and consequently its mode shape, but also its wavelength dependence or dispersion and even its birefringence. Ultra-narrowband filters [48], ultra-broadband couplers [45], ultra-broadband mode converter and de/multiplexer [49], polarization management structures [50] or highly efficient fiber-to-chip couplers [51], are only some examples of recently proposed devices based on this concept [52]. The main limiting factor of SWG technology in the near infrared band has been the difficulty of achieving the required device dimensions compatible with the available minimum feature sizes. However, with the continuous improvement of lithographic processes, already capable of achieving sub-100 nm patterning resolutions, opens an encouraging scenario for the coming years [53].

As an example of propagation in the SWG regime, a cut of the fundamental TE Floquet-Bloch mode is shown in Fig. 7. Due to the segmentation, a significant delocalization of the electric field in comparison with a photonic wire of same dimensions takes place. Furthermore, apart from the field enhancement that occurs at the sidewalls (like in a photonic wire waveguide), the field is also enhanced between the silicon blocks. This enhanced light-matter interaction is the cause of the high sensing capabilities of SWG waveguides.

4.2. The subwavelength grating as sensing waveguide

SWG waveguides were first proposed for biosensing purposes in [18]. It was theoretically shown that such waveguides exhibited sensitivities for TE-polarization that exceed those of conventional Si-photonic wires by a factor of 6 and 2 for TE and TM polarization, respectively. Several groups have incorporated SWG waveguides into their sensing architectures [23,19–22], and have experimentally validated their superior performance. Nevertheless, none of the published works has so far carried out a detailed study of the sensitivity of SWG waveguides as a function of their geometrical parameters. Indeed, the dimensions of standard Si-wires waveguides typically used in telecom applications were directly trans-

ferred to SWG waveguides, i.e. $W = 450$ nm and $H = 220$ nm, which may be sub-optimal from a sensitivity point of view. In this subsection we will calculate both bulk and surface sensitivities for a wide range of geometrical parameters. We will focus on TE polarization at the wavelength of 1550 nm for the SOI platform.

The bulk and surface waveguide sensitivities that will be presented in the following were calculated by applying their respective definitions (see Eq. (6) and (7)), i.e., producing a small variation in the refractive index of the surrounding aqueous solution (bulk case) or an small increment in the thickness of the adsorbed molecular layer (surface case), and recording the variation in the effective index (Δn_{eff}) of the fundamental Floquet-Bloch mode. For the bulk case, the refractive index of the aqueous solution was varied from 1.32 to 1.34, while for the surface case a protein layer with refractive index of 1.45 and variable thickness ranging from 0 to 10 nm was assumed. The protein adlayer was situated in all the surfaces in contact with the aqueous solution, i.e., not only in the five faces of the silicon blocks but also in the interface between the upper cladding and BOX. The effective index of the Floquet mode was calculated by implementing the same procedure used in [18].

The results for the bulk case are shown in Fig. 8(a)–(c), for three different widths ($W = 350, 400, 450$ nm) and silicon thicknesses ($H = 220, 260$ and 300 nm), as a function of the duty cycle. To assist in the physical interpretation of the observed behavior the effective index (n_{eff}) of the fundamental Floquet-Bloch mode has also been plotted. In all cases, a pitch (Λ) of 250 nm was used to ensure that the structure always operates in the SWG regime, i.e., no Bragg reflection occurs. Regarding the constraint of the fabrication process, a minimum feature size of 75 nm has been assumed, which can be realized with e-beam technology. This restricts the DC to the range between $DC = 0.3$ (silicon blocks of length 75 nm) and $DC = 0.7$ (gaps of length of 75 nm), indicated with a labeled arrow in the subfigures. On the other hand, to guarantee negligible leakage loss when operating under weak optical waveguiding conditions, we have used the simple and practical criterion experimentally demonstrated in [54], which establishes that, for BOX thickness of 3 µm, it is enough to maintain the mode effective index above 1.55. This recommended limit is shown in all subfigures as a horizontal line.

From Fig. 8(a)–(c) it is clear that the effective index of the mode can be engineered by modifying any of the geometrical parameters that affect the volume of the silicon blocks, i.e., the height (H), the duty cycle (DC) or the width (W). Accordingly, a reduction in any of them should delocalize the mode field from the silicon blocks and increase the bulk sensitivity. However, since the refractive index of the SiO$_2$ BOX is higher than that of water (1.44 versus 1.32), when reducing the dimensions of the silicon blocks, two effects occur simultaneously: (i) the mode volume progressively increases, enhancing sensitivity and (ii) the mode is displaced towards the BOX, reducing sensitivity. Obviously, there is a point of maximum sensitivity in which both effects mutually compensate. This

phenomenon is clearly observed in all the blue curves shown in Fig. 8(a)–(c). For further insight, the electric field intensity is shown, for different duty-cycles, in Fig. 9. Notice that the case of $DC = 1$ corresponds to the conventional photonic wire.

From the design point of view is very interesting to highlight that in Fig. 8(a)–(c) for all considered widths, heights and duty cycles, the point of maximum sensitivity has an associated value of effective index which is far from the threshold value at which leakage losses start to be significant ($n_{\mathrm{eff}} < 1.55$). For example, for $W = 350$ nm, the effective indexes at the points of maximum sensitivities are $1.64, 1.69$ and 1.72, for $H = 220$ nm, 260 nm and 300 nm, respectively.

Next, we will analyze the dependence of bulk sensibility on the thickness of the silicon layers. In photonic wires ($DC = 1$), it is well known that to enhance the sensitivity, it is convenient to operate with thin layers to push the field out of the waveguide core. Surprisingly in SWG waveguides a thicker silicon layer has remarkable benefits, as can be seen in Fig. 8. The point of maximum sensitivity is shifted closer towards duty-cycles of 50%, which are easier to fabricate, and the maximum achievable sensitivity increases. Additionally, the leakage loss margin defined in terms of effective index increases slightly. For example, a SWG waveguide operating with the typical standard dimensions of photonic wires ($W = 450$ nm; $H = 220$ nm) would achieve a maximum bulk sensitivity of 0.78 RIU/RIU for a $DC = 0.7$, just at the edge of feasible margin of DC. However, by increasing the thickness to a value of 300 nm, a bulk sensitivity as high as 0.9 RIU/RIU would be possible for a $DC = 0.6$.

We finally note that incrementing the waveguide width shifts the sensitivity maximum closer to 50% duty-cycles, at the expense of a slight reduction in the maximum sensitivity value.

In summary, the $H = 220$ nm thickness typically used in telecom applications is not optimum for SWG sensing; thicker silicon layers provide higher sensitivity with duty-cycles that are closer to 50%.

The results for surface sensitivity are shown in Fig. 10(a) and (b), for different heights and widths. We observe that surface sensitivity is enhanced as the duty-cycle is increased, because this enlargens the area of the sidewalls, where the electric field is strongest. The field at the sidewalls is stronger in narrower waveguides, which is why the surface sensitivity experiences a stronger enhancement in narrow waveguides when the duty-cycle is increased.

4.3. Performance metrics of the SWG based biosensors

Since SWG structures were proposed for the first time as sensing waveguides in [18], several groups have experimentally demonstrated their potential. Table 1 summarizes the main characteristics and performance metrics of the most relevant contributions published to date. All works make use of ring resonator architectures. Some classical and highly cited papers using conventional waveguides have also been included in the table as reference
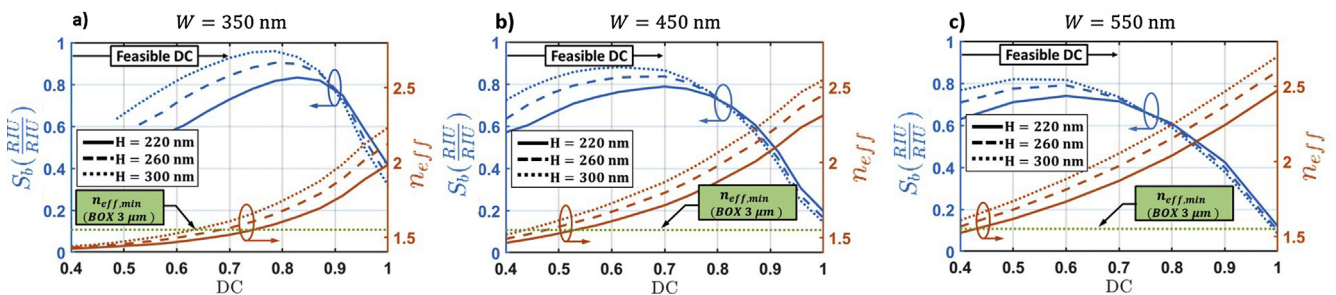

Fig. 8. Bulk sensitivity of SWG waveguide as a function of duty cycle for three different widths: (a) $W = 350$ nm (b) $W = 450$ nm and (c) $W = 550$ nm. For each width, three different standard heights H have been considered: 220 nm, 260 nm and 300 nm. To assist in their physical interpretation, the respective effective indexes of the fundamental Floquet-Bloch are also shown. Other simulation parameters: TE-polarization; $\Lambda = 250$ nm; $\lambda_o = 1550$ nm.
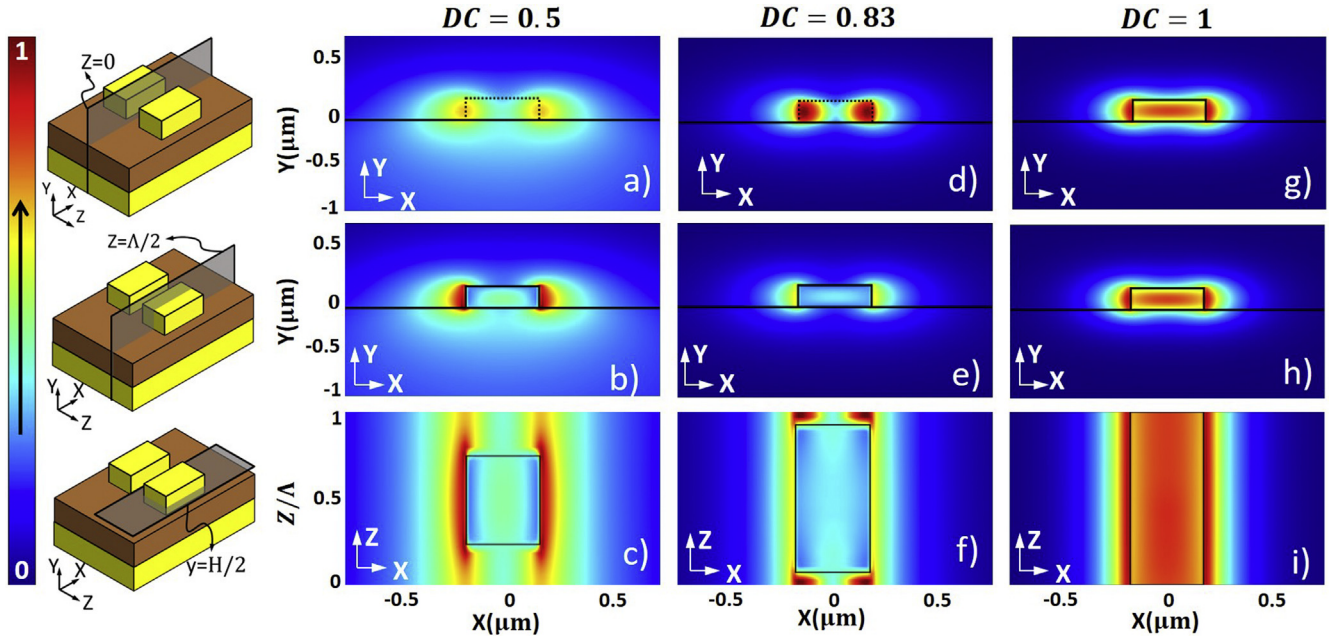
Fig. 9. Evolution of the electric field distribution in three planes (shown in the left column) when varying the duty cycle (DC) in a SWG waveguide. The geometrical parameters were set as follows: $W = 350$ nm; $H = 220$ nm; $\Lambda = 250$ nm.
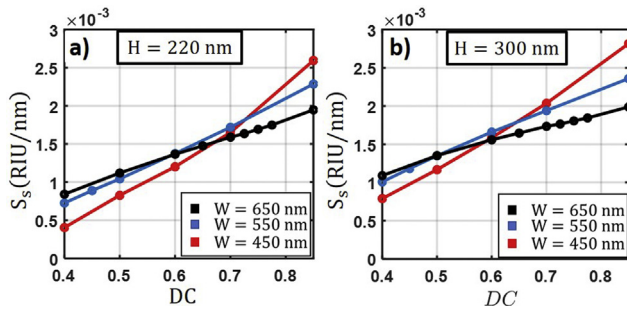

Fig. 10. Surface sensitivity of SWG waveguide as a function of duty cycle for: (a) $H = 220$ nm and different widths ($W = 450$ nm; 550 nm and 650 nm); (b) $H = 300$ nm and different widths ($W = 450$ nm; 550 nm and 650 nm). Other simulation parameters: TE-polarization; $\lambda_0 = 1550$ nm and $\Lambda = 250$ nm.

values: the TE-polarized photonic wire [14], the TM-polarized photonic wire [15] and TE-polarized slot waveguide [17]. We note that the first of them is the sensing system employed by Genalyte [55], a commercially available platform capable of performing complete diagnostic services from a single blood drop in only 15 min. Using SWG structures in ring resonator architectures offers a significant increase of sensitivity, as shown in the results summarized in Table 1. However, to the authors knowledge, interferometric architectures with SWG waveguides have not yet been experimentally demonstrated. Since the enhanced waveguide sensitivity afforded by SWG structures benefits both kinds of architectures, the development of SWG based interferometric biosensors with coherent phase read-out can pave the way for achieving low cost and high sensitivity photonic biosensors.

5. New opportunities for the SWG waveguides in the mid-infrared band

5.1. Why the mid-infrared band?

Up to this point, we have focused on detection of biological substances using light with near-infrared wavelengths. For the detection of hazardous gases the mid-infrared band (wavelengths between 2 μm and 20 μm), is currently attracting a lot of attention from the scientific community [56,57], because the fingerprint region is located in this wavelength range [58]. In this region, vibrational and rotational quantum transitions generate unique absorption peaks which can be used to detect and identify molecules. Indeed, using the principle of evanescent field sensing in the fingerprint region it is possible to obtain the absorbance of a gas analyte in a mixture, and hence its concentration, by simply measuring the optical power attenuation in a waveguide. Since the specific absorption spectrum unequivocally determines the presence of a given molecule, mid-infrared biosensing waveguides are self-selective and do not need functionalization layers. So, it is expected that a plethora of applications will be fully developed in the coming years with the aim of sensing multiple substances, including greenhouse gases, petroleum by-products and pollutants.

5.2. Characterization of sensing waveguides in the mid-infrared band

The power P at the end of an optical waveguide with effective index n_{eff} can be calculated as

$$P = P_0 e^{-2\alpha L}, \tag{22}$$

where P_0 is the input power, L is the length of the waveguide and α is the modal attenuation constant, which includes all sources of power loss (i.e. scattering, radiation and material absorption) and can be calculated as $\alpha = 2\pi\text{Im}(n_{\text{eff}})/\lambda_0$. When the waveguide is used for evanescent-field gas sensing and the cladding contains molecules with vibration-rotation absorption at λ_0, the attenuation constant can be decomposed as a sum of two terms:

$$\alpha = \eta\alpha_{\text{gas}} + \alpha_w, \tag{23}$$

where α_{gas}; is the absorption coefficient of the gas, η is the interaction factor of the evanescent mode field with the gas and α_w denotes the intrinsic propagation loss of the waveguide in the absence of the gas. According to the Beer-Lambert law [59], which we can assume

Table 1
Comparison of SWG based ring resonator architectures ($\lambda_o = 1550$ nm). iLoD has been calculated by using the expression (18).

Ref	Pol.	Platform $W \times H$	Λ	DC	Type of sensing	Waveguide Sensitivity (S_w)	Device Sensitivity (S)	Q ($\times 10^3$)	iLoD	Comments
[14]	TE	500×220 nm² Photonic Wire	–	–	Bulk and Surface	$S_{w,bulk} = 0.16$ RIU/RIU $S_{w,surf} = 0.45$ mRIU/nm	$S_{bulk} = 70$ nm/RIU	20	Bulk: $1.1 \cdot 10^{-3}$ RIU	Microarray chip capable of acquiring up to 128 optical biosensors.
[15]	TM	450×260 nm² Photonic Wire	–	–	Bulk and Surface	$S_{w,bulk} = 0.37$ RIU/RIU $S_{w,surf} = 0.8$ mRIU/nm	$S_{bulk} \approx 200$ nm/RIU	–		
[17]	TE	$H = 220$ nm Slot Waveguide	–	–	Bulk and Surface	$S_{w,bulk} = 0.83$ RIU/RIU $S_{w,surf} = 1.6$ mRIU/nm	$S_{bulk} = 298$ nm/RIU	1.4	Bulk: $3.7 \cdot 10^{-3}$ RIU	Measurements in water
[19]	TE	500×220 nm² SWG	250 nm	0.8	Bulk	$S_{w,bulk} = 0.45$ RIU/RIU	$S_{bulk} = 383$ nm/RIU	3.9	Bulk: $0.99 \cdot 10^{-3}$ RIU	Measurements in salt solutions and bio-molecular binding
[20]	TE	500×220 nm² SWG	250 nm	0.6	Bulk and Surface	Not Available	$S_{bulk} = 490$ nm/RIU $S_{surf} = 0.8$ nm/nm	7	Bulk: $5.5 \cdot 10^{-4}$ RIU	
[21]	TE	450×220 nm² SWG	200 nm	0.65	Bulk and Surface	$S_{w,surf} = 2$ mRIU/nm	$S_{bulk} = 440$ nm/RIU $S_{surf} = 1$ nm/nm	9.1	Bulk: $3.9 \cdot 10^{-4}$ RIU Surf: $0.17 \cdot 10^{-4}$ nm	Shows that the sensitivity remains high as the adlayer thickness grows.
[22]	TM	600×220 nm² SWG	200 nm	0.7	Bulk	Not Available	$S_{bulk} = 430$ nm/RIU	9.8	Bulk: $3.7 \cdot 10^{-4}$ RIU	Explore the TM mode in SWG based racetrack resonators.

valid in most practical uses of evanescent field-based sensing in the MIR, we can state that

$$\alpha_{gas} = \frac{\varepsilon c}{2}, \tag{24}$$

with ε the molar absorption coefficient of the gas and c its concentration, so that Eq. (22) becomes

$$P = P_0 e^{-\eta \varepsilon c L - 2\alpha_w L}. \tag{25}$$

This expression shows how the concentration c of a specific substance can be obtained by measuring the power drop at the output of the waveguide.

The primary figure of merit of an evanescent field sensor is its sensitivity to changes in the concentration of the gas under examination. Taking derivatives of Eq. (25), this parameter can be defined as

$$S = \frac{\partial P}{\partial c} = -\eta \varepsilon L P, \tag{26}$$

Applying the chain rule and making use of Eqs. (22) and (24), the sensitivity of Eq. (26) can be reinterpreted as

$$S = \frac{\partial P}{\partial c} = \frac{\partial P}{\partial \alpha} \cdot \frac{\partial \alpha}{\partial \alpha_{gas}} \cdot \frac{\partial \alpha_{gas}}{\partial c} = S_a S_w \frac{\varepsilon}{2}, \tag{27}$$

where $S_a = \partial P / \partial \alpha = -2LP$ is the architecture sensitivity of the system and $S_w = \eta = \partial \alpha / \partial \alpha_{gas}$ is the waveguide sensitivity. Eq. (27) indicates that, for a given substance (ε), sensitivity will be higher if the interaction with the evanescent field is maximized, which can be achieved by increasing the waveguide sensitivity S_w or enlarging the path length L. Furthermore, the intrinsic propagation losses of the waveguide α_w, included in S_a through P, limit the detection functionality of the sensor because they act as a spurious source of absorption that can even render the sensor useless if output power falls under the minimum detectable. The factor S_w determines the intrinsic sensitivity of the waveguide without taking into account the specific substance that will be sensed (ε) or the system architecture (length L and loss α_w). Consequently, even though Eq. (27) is an appropriate definition from an experimental point of view, in this work we will utilize the waveguide sensitivity S_w as the main performance metric. At this point it is important to remark that the interaction factor $\eta = S_w$ is commonly expressed as a confinement factor [60]

$$\Gamma_{gas} = \frac{\int_{sensing\ cladding} S_z(x,y)dxdy}{\int_{overall\ waveguide\ cross-section} S_z(x,y)dxdy}, \tag{28}$$

with $S_z(x,y)$ the time average of the longitudinal component of the Poynting vector. However, although Eq. (28) is a good approximation for η in low contrast fabrication technologies (e.g. silica or polymers), it cannot be applied to estimate the sensitivity of waveguides in high contrast platforms, such as silicon-on-insulator [61,62]. Thus, we will simply use

$$S_w = \frac{\partial \alpha}{\partial \alpha_{gas}}. \tag{29}$$

Note that this definition is the evanescent field absorption counterpart of Eq. (6), where we studied the variation of the real part of the mode effective index with respect to the refractive index. Now we will analyze the variation of the imaginary part with respect to the attenuation constant of the gas.

5.3. The suspended silicon waveguide with subwavelength grating cladding: calculation of its sensitivity

Silicon-on-insulator (SOI) is the most used platform in silicon photonics at NIR wavelengths since it allows high integrability

with cost efficiency and mass production compatible with traditional microelectronics fabrication processes [56]. These advantages remain valid when moving towards higher wavelengths, making SOI an excellent candidate for ultra-compact lab-on-chip optical circuits in the MIR. Nevertheless, silicon dioxide, the typical insulator in SOI wafers, exhibits unacceptable material losses for wavelengths greater than 4 μm [57], jeopardizing the suitability of this platform in the long-wave range. Several research groups have proposed alternatives to the conventional SOI platform where SiO_2 is removed [63,64] or is substituted with other materials such as sapphire [65] or silicon nitride [66]. Recently, it has been experimentally reported suspended silicon waveguides for $\lambda_0 = 3.8$ μm [67,68] and $\lambda_0 = 7.67$ μm [69] with propagation losses as low as $\alpha_w = 0.82$ dB/cm and 3.1 dB/cm, respectively. The geometry of these structures is represented in Fig. 11. In this waveguiding platform, the buried oxide layer (BOX) of thickness H_{BOX} is eliminated by using hydrofluoric (HF) acid, extending the theoretical operation range up to 8.5 μm, the transparency limit of silicon itself. To fabricate these waveguides, a first dry etch step is applied to make holes of length L_{hole} in the Si layer. After that, the structure is attacked with HF, which removes the SiO_2 through the holes. In this way, the silicon waveguide core (width W_{core} and height H_{core}) is suspended, only anchored to the remaining lateral silicon walls by a series of silicon strips of length L_{Si}. In addition to holding the waveguide core and providing mechanical stability, these strips have an optical function: conveniently designed, they work as a SWG cladding of width W_{clad} that provides the index contrast required for waveguiding. Due to holes in the cladding and the absence of a BOX layer, the amount of evanescent field that can be in contact with an analyte gas is higher than in conventional waveguides. This makes suspended waveguides strong candidates for mid-infrared on-chip spectroscopy.

This kind of waveguides can, however, suffer from power leakage from the core to the silicon substrate and to the lateral silicon slabs. The waveguides were designed for the TE polarization to minimize propagation losses by avoiding both sources of leakage. At $\lambda_0 = 3.8$ μm, with a SOI wafer of $H_{core} = 0.5$ μm and $H_{BOX} = 3$ μm, this is accomplished for $W_{core} = 1.3$ μm, $W_{clad} = 2.5$ μm, $L_{Si} = 0.1$ μm and $L_{hole} = 0.45$ μm, delivering measured propagation losses of only 0.82 dB/cm. At $\lambda_0 = 7.67$ μm, although the Si thickness was scaled up to $H_{core} = 1.4$ μm, H_{BOX} remained equal to 3 μm. As a result, a full redesign was required, both to allow practical single-mode operation and to prevent the structure from collapsing. With $W_{core} = 2.9$ μm, $W_{clad} = 3$ μm, $L_{Si} = 0.25$ μm and $L_{hole} = 0.9$ μm, a low propagation loss of 3.1 dB/cm was measured. Note that the higher loss of this waveguide

with respect to its $\lambda_0 = 3.8$ μm counterpart is primarily due to the intrinsic losses of silicon ($\alpha_{Si} \approx 2$ dB/cm at $\lambda_0 = 7.67$ μm [70]). Fig. 12 shows the transverse field profiles of the fundamental TE and TM for $\lambda_0 = 3.8$ μm and $\lambda_0 = 7.67$ μm suspended waveguides, simulated with RSoft™ and Photon Design® software tools. For TM modes (right column) the electric field is further expanded out of the Si core than for TE modes (left column), so that the interaction with the analyte will be stronger. Therefore, in terms of waveguide sensitivity, TM modes are preferable over TE modes. However, if H_{BOX} and W_{clad} are too small, the evanescent field tails can reach the silicon substrate and the non-suspended lateral silicon slabs vastly increasing the intrinsic waveguide losses as a result of leakage. Thus, as shown in Fig. 12(b), at $\lambda_0 = 3.8$ μm the TM mode is so weakly guided that, regardless of its high S_w value, the waveguide turns out to be unable for sensing applications. Consequently, and also because the absorption band of many substances of interest (e.g. CH_4) is around 7.6 μm, we will focus on the long-wave wavelength suspended waveguide with TM polarization. In that case,
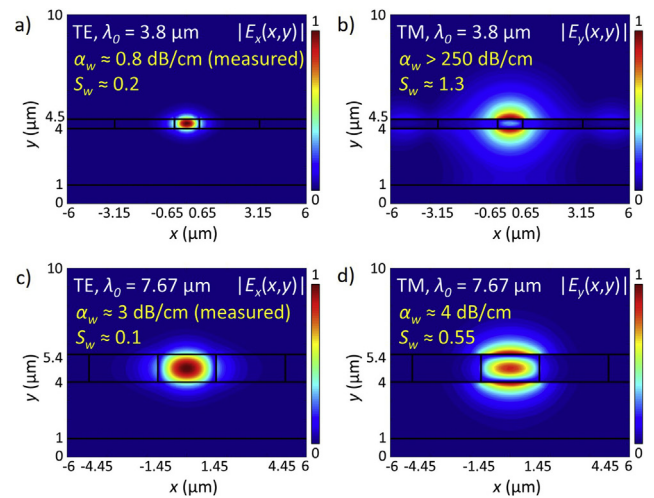
Fig. 12. Transversal mode field distributions for (a) TE and (b) TM polarizations at $\lambda_0 = 3.8$ μm and for (c) TE and (d) TM polarizations at $\lambda_0 = 7.67$ μm. Intrinsic propagation losses and waveguides sensitivities are indicated. For TE polarization α_w values are experimental, whereas for TM polarization they are simulated.
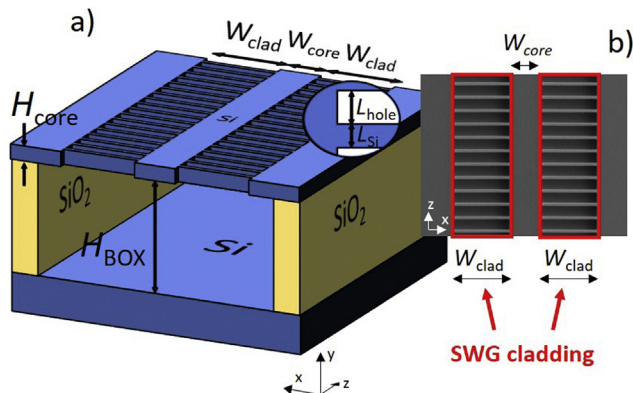
Fig. 11. (a) Schematic 3D representation of a suspended waveguide. Inset: zoom of the SWG cladding strips and holes. (b) SEM image of a fabricated silicon suspended waveguide operating at $\lambda_0 = 3.8$ μm (top view).
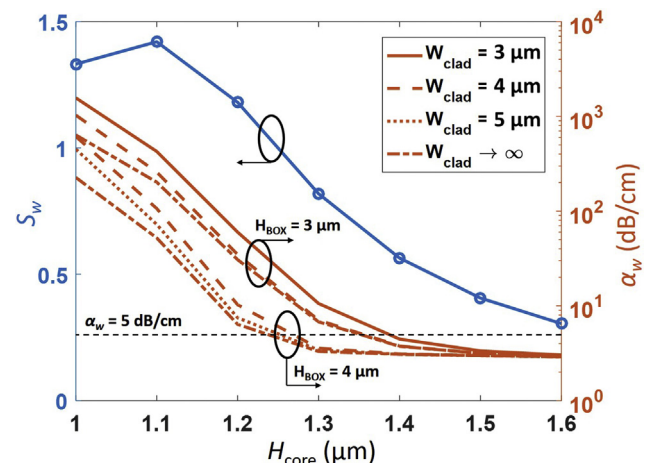
Fig. 13. Simulated waveguide sensitivity as a function of the core thickness (left axis). Simulated propagation losses (leakage losses to substrate and lateral silicon, as well as material losses) as a function of the core thickness for several cladding widths (right axis). TM polarization at $\lambda_0 = 7.67$ μm is considered.

the suspended waveguide exhibits a sensitivity $S_w \approx 0.55$, noticeably higher than sensitivities for the TE modes at $\lambda_0 = 3.8$ μm ($S_w \approx 0.2$) and $\lambda_0 = 7.67$ μm ($S_w \approx 0.1$).

As these suspended waveguides were originally designed with the aim of minimizing losses, but not of maximizing sensitivity, it is worth to study how the latter is affected by variations in the waveguide thickness core H_{core}. Fig. 13 shows the sensitivity S_w as a function of H_{core} for TM polarization at $\lambda_0 = 7.67$ μm. Intrinsic waveguide propagation losses are also represented for several H_{BOX} thicknesses and W_{clad} widths. Boundary cases where lateral leakage is neglected ($W_{clad} \to \infty$) are also included to show the minimum achievable loss for each H_{core}. For $H_{core} = 1.1$ μm waveguide sensitivity is clearly optimized ($S_w \approx 1.4$), but leakage losses are excessively high in all depicted cases. Setting $\alpha_w = 5$ dB/cm as the maximum acceptable loss, in the best-case scenario ($W_{clad} \to \infty$) sensitivity could be improved to 0.7 for $H_{core} = \sim 1.35$ μm. This can be practically achieved with a $W_{clad} = 4$ μm wide cladding. If H_{BOX} were increased to 4 μm, sensitivities of $S_w \approx 0.9$ for $W_{clad} = 4$ μm and $H_{core} = 1.27$ μm, and $S_w \approx 1$ for $W_{clad} = 5$ μm and $H_{core} = 1.24$ μm could be obtained. For this latter case, allowing $\alpha_w = 7$ dB/cm, sensitivities as high as ~ 1.2 might be delivered with $H_{core} \approx 1.2$ μm. Suspended waveguides are thus extremely promising candidates for evanescent field absorption-based sensors in the MIR.

6. Conclusions

We have reviewed the main parameters determining the sensitivity of photonic biosensors, highlighting that interferometric sensors with coherent phase read-out constitute a simple yet accurate sensor architecture. The use of subwavelength structures in sensing waveguide enhances their sensitivity both for biosensing in the near infrared and for absorption spectroscopy in the mid-infrared. In both scenarios, significant enhancement can be achieved by optimizing the waveguide geometry for sensitivity. We are confident that with a holistic sensor design approach today's already excellent sensitivities can be further improved.

Acknowledgments

References

[1] A.F. Gavela, D.G. García, J. Ramirez, L. Lechuga, Last advances in silicon-based optical biosensors, Sensors 16 (3) (2016) 285, https://doi.org/10.3390/s16030285.

[2] A.Z. Subramanian, E. Ryckeboer, A. Dhakal, F. Peyskens, A. Malik, B. Kuyken, H. Zhao, S. Pathak, A. Ruocco, A.D. Groote, P. Wuytens, D. Martens, F. Leo, W. Xie, U.D. Dave, M. Muneeb, P.V. Dorpe, J.V. Campenhout, W. Bogaerts, P. Bienstman, N.L. Thomas, D.V. Thourhout, Z. Hens, G. Roelkens, R. Baets, Silicon and silicon nitride photonic circuits for spectroscopic sensing on-a-chip [invited], Photon. Res. 3 (5) (2015) B47, https://doi.org/10.1364/prj.3.000b47.

[3] S.M. Yoo, S.Y. Lee, Optical biosensors for the detection of pathogenic microorganisms, Trends Biotechnol. 34 (2016) 7–25, https://doi.org/10.1016/j.tibtech.2015.09.012.

[4] M. Soler, P. Mesa-Antunez, M.-C. Estevez, A.J. Ruiz-Sanchez, M.A. Otte, B. Sepulveda, D. Collado, C. Mayorga, M.J. Torres, E. Perez-Inestrosa, L.M. Lechuga, Highly sensitive dendrimer-based nanoplasmonic biosensor for drug allergy diagnosis, Biosensors Bioelectron. 66 (2015) 115–123, https://doi.org/10.1016/j.bios.2014.10.081.

[5] A.L. Washburn, M.S. Luchansky, A.L. Bowman, R.C. Bailey, Quantitative, label-free detection of five protein biomarkers using multiplexed arrays of silicon photonic microring resonators, Anal. Chem. 82 (2010) 69–72, https://doi.org/10.1021/ac902451b.

[6] Y. Fang, Label-free drug discovery, Front. Pharmacol. 5 (2014) 52, https://doi.org/10.3389/fphar.2014.00052.

[7] J.-P. Renaud, C.-W. Chung, U.H. Danielson, U. Egner, M. Hennig, R.E. Hubbard, H. Nar, Biophysics in drug discovery: impact, challenges and opportunities, Nat. Rev. Drug Discov. 15 (2016) 679–698, https://doi.org/10.1038/nrd.2016.123.

[8] M.C. Estevez, M. Alvarez, L.M. Lechuga, Integrated optical devices for lab-on-a-chip biosensing applications, Laser Photon. Rev. 6 (4) (2012) 463–487, https://doi.org/10.1002/lpor.201100025.

[9] A. Densmore, D.X. Xu, P. Waldron, S. Janz, P. Cheben, J. Lapointe, A. Delge, B. Lamontagne, J.H. Schmid, E. Post, A silicon-on-insulator photonic wire based evanescent field sensor, IEEE Photon. Technol. Lett. 18 (23) (2006) 2520–2522, https://doi.org/10.1109/lpt.2006.887374.

[10] V. Passaro, F. Dell'Olio, B. Casamassima, F.D. Leonardis, Guided-wave optical biosensors, Sensors 7 (4) (2007) 508–536, https://doi.org/10.3390/s7040508.

[11] I.M. White, X. Fan, On the performance quantification of resonant refractive index sensors, Opt. Express 16 (2) (2008) 1020–1028, https://doi.org/10.1364/OE.16.001020.

[12] L. Chrostowski, S. Grist, J. Flueckiger, W. Shi, X. Wang, E. Ouellet, H. Yun, M. Webb, B. Nie, Z. Liang, et al., Silicon photonic resonator sensors and devices (feb 2012). https://doi.org/10.1117/12.916860.

[13] K. Zinoviev, A. González-Guerrero, C. Domínguez, L. Lechuga, Integrated bimodal waveguide interferometric biosensor for label-free analysis, J. Lightwave Technol. 29 (13) (2011) 1926–1930, https://doi.org/10.1109/JLT.2011.2150734.

[14] K. De Vos, I. Bartolozzi, E. Schacht, P. Bienstman, R. Baets, Silicon-on-insulator microring resonator for sensitive and label-free biosensing, Opt. Express 15 (12) (2007) 7610, https://doi.org/10.1364/oe.15.007610.

[15] S. Janz, D.-X. Xu, M. Vachon, N. Sabourin, P. Cheben, H. McIntosh, H. Ding, S. Wang, J.H. Schmid, A. Delâge, J. Lapointe, A. Densmore, R. Ma, W. Sinclair, S. Logan, R. MacKenzie, Q. Liu, D. Zhang, G. Lopinski, O. Mozenson, M. Gilmour, H. Tabor, Photonic wire biosensor microarray chip and instrumentation with application to serotyping of Escherichia coli isolates, Opt. Express 21 (4) (2013) 4623, https://doi.org/10.1364/oe.21.004623.

[16] F. Dell'Olio, V.M. Passaro, Optical sensing by optimized silicon slot waveguides, Opt. Express 15 (8) (2007) 4977, https://doi.org/10.1364/oe.15.004977.

[17] T. Claes, J. Molera, K.D. Vos, E. Schacht, R. Baets, P. Bienstman, Label-free biosensing with a slot-waveguide-based ring resonator in silicon on insulator, IEEE Photon. J. 1 (3) (2009) 197–204, https://doi.org/10.1109/jphot.2009.2031596.

[18] J.G. Wangüemert-Pérez, P. Cheben, A. Ortega-Moñux, C. Alonso-Ramos, D. Pérez-Galacho, R. Halir, Í. Molina-Fernández, D.-X. Xu, J.H. Schmid, Evanescent field waveguide sensing with subwavelength grating structures in silicon-on-insulator, Opt. Lett. 39 (2014) 4442–4445, https://doi.org/10.1364/OL.39.004442.

[19] V. Donzella, A. Sherwali, J. Flueckiger, S.M. Grist, S.T. Fard, L. Chrostowski, Design and fabrication of SOI micro-ring resonators based on sub-wavelength grating waveguides, Opt. Express 23 (2015) 4791–4803, https://doi.org/10.1364/OE.23.004791.

[20] J. Flueckiger, S. Schmidt, V. Donzella, A. Sherwali, D.M. Ratner, L. Chrostowski, K.C. Cheung, Sub-wavelength grating for enhanced ring resonator biosensor, Opt. Express 24 (2016) 15672–15686, https://doi.org/10.1364/OE.24.015672.

[21] H. Yan, L. Huang, X. Xu, S. Chakravarty, N. Tang, H. Tian, R.T. Chen, Unique surface sensing property and enhanced sensitivity in microring resonator biosensors based on subwavelength grating waveguides, Opt. Express 24 (2016) 29724–29733, https://doi.org/10.1364/OE.24.029724.

[22] L. Huang, H. Yan, X. Xu, S. Chakravarty, N. Tang, H. Tian, R.T. Chen, Improving the detection limit for on-chip photonic sensors based on subwavelength grating racetrack resonators, Opt. Express 25 (2017) 10527–10535, https://doi.org/10.1364/OE.25.010527.

[23] Z. Tu, D. Gao, M. Zhang, D. Zhang, High-sensitivity complex refractive index sensing based on Fano resonance in the subwavelength grating waveguide micro-ring resonator, Opt. Express 25 (2017) 20911–20922, https://doi.org/10.1364/OE.25.020911.

[24] T. Chalyan, R. Guider, L. Pasquardini, M. Zanetti, F. Falke, E. Schreuder, R. Heideman, C. Pederzolli, L. Pavesi, Asymmetric Mach-Zehnder interferometer based biosensors for aflatoxin M1 detection, Biosensors 6 (1) (2016) 1, https://doi.org/10.3390/bios6010001.

[25] A. Densmore, D.-X. Xu, S. Janz, P. Waldron, J. Lapointe, T. Mischki, G. Lopinski, A. Delâge, J.H. Schmid, P. Cheben, Sensitive label-free biomolecular detection using thin silicon waveguides, Adv. Opt. Technol. 2008 (2008) 1–9, https://doi.org/10.1155/2008/725967.

[26] S. Dante, D. Duval, B. Sepúlveda, A.B. González-Guerrero, J.R. Sendra, L.M. Lechuga, All-optical phase modulation for integrated interferometric biosensors, Opt. Express 20 (7) (2012) 7195–7205, https://doi.org/10.1364/oe.20.007195.

[27] R. Halir, L. Vivien, X.L. Roux, D.-X. Xu, P. Cheben, Direct and sensitive phase readout for integrated waveguide sensors, IEEE Photon. J. 5 (2013) 6800906, https://doi.org/10.1109/jphot.2013.2276747.

[28] P.J. Reyes-Iglesias, I. Molina-Fernández, A. Moscoso-Mártir, A. Ortega-Moñux, High-performance monolithically integrated 120degr downconverter with relaxed hardware constraints, Opt. Express 20 (5) (2012) 5725–5741, https://doi.org/10.1364/oe.20.005725.

[29] R.J.J. van Gulik, B.M. de Boer, P.J. Harmsma, Refractive index sensing using a three-port interferometer and comparison with ring resonators, IEEE J. Sel. Top. Quant. Electron. 23 (2) (2017) 433–439, https://doi.org/10.1109/jstqe.2016.2601899.

[30] A. Densmore, M. Vachon, D.-X. Xu, S. Janz, R. Ma, Y.-H. Li, G. Lopinski, A. Delâge, J. Lapointe, C.C. Luebbert, Q.Y. Liu, P. Cheben, J.H. Schmid, Silicon photonic wire biosensor array for multiplexed real-time and label-free molecular detection, Opt. Lett. 34 (2009) 3598–3600, https://doi.org/10.1364/OL.34.003598.

[31] N.P. Mauranyapin, L.S. Madsen, M.A. Taylor, M. Waleed, W.P. Bowen, Evanescent single-molecule biosensing with quantum-limited precision, Nat. Photon. 11 (8) (2017) 477–481, https://doi.org/10.1038/nphoton.2017.99.

[32] V. Passaro, F. Dell'Olio, F.D. Leonardis, Ammonia optical sensing by microring resonators, Sensors 7 (11) (2007) 2741–2749, https://doi.org/10.3390/s7112741.

[33] X. Wang, C.K. Madsen, Highly sensitive compact refractive index sensor based on phase-shifted sidewall Bragg gratings in slot waveguide, Appl. Opt. 53 (2014) 96–103, https://doi.org/10.1364/AO.53.000096.

[34] S.M. Grist, S.A. Schmidt, J. Flueckiger, V. Donzella, W. Shi, S. Talebi Fard, J.T. Kirk, D.M. Ratner, K.C. Cheung, L. Chrostowski, Silicon photonic micro-disk resonators for label-free biosensing, Opt. Express 21 (2013) 7994–8006, https://doi.org/10.1364/OE.21.007994.

[35] D.X. Xu, A. Densmore, A. Delâge, P. Waldron, R. McKinnon, S. Janz, J. Lapointe, G. Lopinski, T. Mischki, E. Post, P. Cheben, J.H. Schmid, Folded cavity SOI microring sensors for high sensitivity and real time measurement of biomolecular binding, Opt. Express 16 (2008) 15137–15148, https://doi.org/10.1364/oe.16.015137.

[36] D.-X. Xu, M. Vachon, A. Densmore, R. Ma, S. Janz, A. Delâge, J. Lapointe, P. Cheben, J.H. Schmid, E. Post, S. Messaoud̀nne, J.-M. Fédéli, Real-time cancellation of temperature induced resonance shifts in SOI wire waveguide ring resonator label-free biosensor arrays, Opt. Express 18 (2010) 22867–22879, https://doi.org/10.1364/OE.18.022867.

[37] R. Halir, P. Cheben, S. Janz, D.-X. Xu, i. Molina-Fernández, J.G. Wangüemert-Pérez, Waveguide grating coupler with subwavelength microstructures, Opt. Lett. 34 (9) (2009) 1408–1410, https://doi.org/10.1364/ol.34.001408.

[38] R. Halir, P. Cheben, J.H. Schmid, R. Ma, D. Bedard, S. Janz, D.-X. Xu, A. Densmore, J. Lapointe, I. Molina-Fernández, Continuously apodized fiber-to-chip surface grating coupler with refractive index engineered subwavelength structure, Opt. Lett. 35 (19) (2010) 3243–3245, https://doi.org/10.1364/ol.35.003243.

[39] R. Halir, L. Zavargo-Peche, D.-X. Xu, P. Cheben, R. Ma, J.H. Schmid, S. Janz, A. Densmore, A. Ortega-Moñux, Í. Molina-Fernández, M. Fournier, J.-M. Fédeli, Single etch grating couplers for mass fabrication with DUV lithography, Opt. Quant. Electron. 44 (12) (2012) 521–526, https://doi.org/10.1007/s11082-012-9563-2.

[40] P.J. Reyes-Iglesias, A. Ortega-Moñux, I. Molina-Fernández, Colorless monolithically integrated 120° downconverter, Opt. Express 21 (2013) 23048–23057, https://doi.org/10.1364/OE.21.023048.

[41] L.B. Soldano, E.C.M. Pennings, Optical multi-mode interference devices based on self-imaging: principles and applications, J. Lightwave Technol. 13 (4) (1995) 615–627, https://doi.org/10.1109/50.372474.

[42] J. Milvich, D. Kohler, W. Freude, C. Koos, Mach-zehnder interferometer readout for instantaneous sensor calibration and extraction of endlessly unwrapped phase, in: Proc. IEEE Photonics Conf. (IPC), 2017, pp. 567–568. https://doi.org/10.1109/IPCon.2017.8116226.

[43] D. Duval, A.B. González-Guerrero, S. Dante, J. Osmond, R. Monge, L.J. Fernández, K.E. Zinoviev, C. Domínguez, L.M. Lechuga, Nanophotonic lab-on-a-chip platforms including novel bimodal interferometers, microfluidics and grating couplers, Lab Chip 12 (11) (2012) 1987, https://doi.org/10.1039/c2lc40054e.

[44] F. Prieto, B. Sepúlveda, A. Calle, A. Llobera, C. Domínguez, A. Abad, A. Montoya, L.M. Lechuga, An integrated optical interferometric nanodevice based on silicon technology for biosensor applications, Nanotechnology 14 (8) (2003) 907. http://stacks.iop.org/0957-4484/14/i=8/a=312.

[45] R. Halir, P. Cheben, J.M. Luque-González, J.D. Sarmiento-Merenguel, J.H. Schmid, G. Wangüemert-Pérez, D.-X. Xu, S. Wang, A. Ortega-Moñux, Í. Molina-Fernández, Ultra-broadband nanophotonic beamsplitter using an anisotropic sub-wavelength metamaterial, Laser Photon. Rev. 10 (6) (2016) 1039–1046, https://doi.org/10.1002/lpor.201600213.

[46] R. Halir, P. Bock, P. Cheben, A. Ortega-Moñux, C. Alonso-Ramos, J. Schmid, J. Lapointe, D.-X. Xu, J. Wangüemert-Pérez, I. Molina-Fernández, S. Janz, Waveguide sub-wavelength structures: a review of principles and applications, Laser Photon. Rev. 9 (1) (2015) 25–49, https://doi.org/10.1002/lpor.201400083.

[47] J. Joannopoulos, S. Johnson, J. Winn, R. Meade, Photonic Crystals: Molding the Flow of Light, Princeton University Press, 2011.

[48] J. Čtyroký, J.G. Wangüemert-Pérez, P. Kwiecien, I. Richter, J. Litvik, J.H. Schmid, Í. Molina-Fernández, A. Ortega-Moñux, M. Dado, P. Cheben, Design of narrowband Bragg spectral filters in subwavelength grating metamaterial waveguides, Opt. Express 26 (1) (2018) 179, https://doi.org/10.1364/oe.26.000179.

[49] D. González-Andrade, J. Wangüemert-Pérez, A. Velasco, A. Ortega-Moñux, A. Herrero-Bermello, I. Molina-Fernández, R. Halir, P. Cheben, Ultra-broadband mode converter and multiplexer based on sub-wavelength structures, IEEE Photon. J. 10 (2) (2018) 1–10, https://doi.org/10.1109/jphot.2018.2819364.

[50] Y. Xiong, J. Wangüemert-Pérez, D.-X. Xu, J. Schmid, P. Cheben, W. Ye, Polarization splitter and rotator with subwavelength grating for enhanced fabrication tolerance, Opt. Lett. 39 (24) (2014) 6931–6934, https://doi.org/10.1364/ol.39.006931.

[51] D. Benedikovic, C. Alonso-Ramos, P. Cheben, J.H. Schmid, S. Wang, D.-X. Xu, J. Lapointe, S. Janz, R. Halir, A. Ortega-Moñux, J.G. Wangüemert-Pérez, I. Molina-Fernández, J.-M. Fédéli, L. Vivien, M. Dado, High-directionality fiber-chip grating coupler with interleaved trenches and subwavelength index-matching structure, Opt. Lett. 40 (2015) 4190–4193, https://doi.org/10.1364/OL.40.004190.

[52] A. Sánchez-Postigo, J.G. Wangüemert-Pérez, J.M. Luque-González, Í. Molina-Fernández, P. Cheben, C.A. Alonso-Ramos, R. Halir, J.H. Schmid, A. Ortega-Moñux, Broadband fiber-chip zero-order surface grating coupler with 04 dB efficiency, Opt. Lett. 41 (13) (2016) 3013, https://doi.org/10.1364/ol.41.003013.

[53] S.-H. Jeong, D. Shimura, T. Simoyama, M. Seki, N. Yokoyama, M. Ohtsuka, K. Koshino, T. Horikawa, Y. Tanaka, K. Morito, Low-loss, flat-topped and spectrally uniform silicon-nanowire-based 5th-order CROW fabricated by ArF-immersion lithography process on a 300-mm SOI wafer, Opt. Express 21 (25) (2013) 30163, https://doi.org/10.1364/oe.21.030163.

[54] J.D. Sarmiento-Merenguel, A. Ortega-Moñux, J.-M. Fédéli, J.G. Wangüemert-Pérez, C. Alonso-Ramos, E. Durán-Valdeiglesias, P. Cheben, i. Molina-Fernández, R. Halir, Controlling leakage losses in subwavelength grating silicon metamaterial waveguides, Opt. Lett. 41 (2016) 3443–3446, https://doi.org/10.1364/OL.41.003443.

[55] Genalyte Inc. URL <http://www.genalyte.com>.

[56] R.A. Soref, S.J. Emelett, W.R. Buchwald, Silicon waveguided components for the long-wave infrared region, J. Opt. A: Pure Appl. Opt. 8 (10) (2006) 840. http://stacks.iop.org/1464-4258/8/i=10/a=004.

[57] R. Soref, Mid-infrared photonics in silicon and germanium, Nat. Photonics 4 (8) (2010) 495–497, https://doi.org/10.1038/nphoton.2010.171.

[58] T. Hu, B. Dong, X. Luo, T.-Y. Liow, J. Song, C. Lee, G.-Q. Lo, Silicon photonic platforms for mid-infrared applications [invited], Photon. Res. 5 (5) (2017) 417, https://doi.org/10.1364/prj.5.000417.

[59] R. Siebert, J. Müller, Infrared integrated optical evanescent field sensor for gas analysis, Sensors Actuat. A: Phys. 119 (1) (2005) 138–149, https://doi.org/10.1016/j.sna.2004.11.001.

[60] B. Kumari, A. Barh, R. Varshney, B. Pal, Silicon-on-nitride slot waveguide: a promising platform as mid-IR trace gas sensor, Sensors Actuat. B: Chem. 236 (2016) 759–764, https://doi.org/10.1016/j.snb.2016.06.060.

[61] T. Visser, H. Blok, B. Demeulenaere, D. Lenstra, Confinement factors and gain in optical amplifiers, IEEE J. Quant. Electron. 33 (10) (1997) 1763–1766, https://doi.org/10.1109/3.631230.

[62] D.B. Li, C.Z. Ning, Peculiar features of confinement factors in a metal-semiconductor waveguide, Appl. Phys. Lett. 96 (18) (2010) 181109, https://doi.org/10.1063/1.3425896.

[63] Z. Cheng, X. Chen, C.Y. Wong, K. Xu, H.K. Tsang, Mid-infrared suspended membrane waveguide and ring resonator on silicon-on-insulator, IEEE Photon. J. 4 (5) (2012) 1510–1519, https://doi.org/10.1109/jphot.2012.2210700.

[64] W. Zhou, Z. Cheng, X. Wu, X. Sun, H.K. Tsang, Fully suspended slot waveguide platform, J. Appl. Phys. 123 (6) (2018) 063103, https://doi.org/10.1063/1.5017780.

[65] T. Baehr-Jones, A. Spott, R. Ilic, A. Spott, B. Penkov, W. Asher, M. Hochberg, Silicon-on-sapphire integrated waveguides for the mid-infrared, Opt. Express 18 (12) (2010) 12127, https://doi.org/10.1364/oe.18.012127.

[66] S. Khan, J. Chiles, J. Ma, S. Fathpour, Silicon-on-nitride waveguides for mid- and near-infrared integrated photonics, Appl. Phys. Lett. 102 (12) (2013) 121104, https://doi.org/10.1063/1.4798557.

[67] J. Soler Penadés, C. Alonso-Ramos, A.Z. Khokhar, M. Nedeljkovic, L.A. Boodhoo, A. Ortega-Moñux, I. Molina-Fernández, P. Cheben, G.Z. Mashanovich, Suspended SOI waveguide with sub-wavelength grating cladding for mid-infrared, Opt. Lett. 39 (19) (2014) 5661, https://doi.org/10.1364/ol.39.005661.

[68] J. Soler Penadés, A. Ortega-Moñux, M. Nedeljkovic, J.G. Wangüemert-Pérez, R. Halir, A.Z. Khokhar, C. Alonso-Ramos, Z. Qu, I. Molina-Fernández, P. Cheben, G.Z. Mashanovich, Suspended silicon mid-infrared waveguide devices with subwavelength grating metamaterial cladding, Opt. Express 24 (20) (2016) 22908, https://doi.org/10.1364/oe.24.022908.

[69] J. Soler Penadés, A. Sánchez-Postigo, M. Nedeljkovic, A. Ortega-Moñux, J.G. Wangüemert-Pérez, Y. Xu, R. Halir, Z. Qu, A.Z. Khokhar, A. Osman, W. Cao, C.G. Littlejohns, P. Cheben, I. Molina-Fernández, G.Z. Mashanovich, Suspended silicon waveguides for long-wave infrared wavelengths, Opt. Lett. 43 (4) (2018) 795, https://doi.org/10.1364/ol.43.000795.

[70] D. Chandler-Horowitz, P.M. Amirtharaj, High-accuracy, midinfrared (450 cm^{-1} ⩽ ω ⩽ 4000 cm^{-1}) refractive index values of silicon, J. Appl. Phys. 97 (12) (2005) 123526, https://doi.org/10.1063/1.1923612.